Effect of stochastic forcing on the dynamic behavior of a self-sustained oscillator coupled to a non-linear energy sink

Baptiste Bergeot

Effect of stochastic forcing on the dynamic behavior of a self-sustained oscillator coupled to a non-linear energy sink

Baptiste Bergeot[a,*]

[a]*INSA CVL, Univ. Orléans, Univ. Tours, LaMé EA 7494, F-41034, 3 Rue de la Chocolaterie, CS 23410, 41034 Blois Cedex, France*

Abstract

In this paper the influence of stochasticity (i.e. a Gaussian white noise forcing) on the dynamic behavior of a self-sustained oscillator coupled to a non-linear energy sink is investigated. To this end, the standard stochastic averaging is used to compute the slow flow dynamics of the system. Preliminary results show that the reasoning which allows to predict the system behavior in the deterministic case can be contradicted in presence of stochasticity. Then, by means of the Monte Carlo method, the stochastic averaging procedure is validated. Finally, two quantities are introduced to highlight more precisely the special features of the stochastic system behavior compared to that of the deterministic system. These are the *probability of being in a harmless regime* and the *First-Passage Time to reach a harmful regime* which are computed and investigated combining again the Monte Carlo approach with numerical integrations of the slow flow dynamics. The results obtained show afresh that the stochastic forcing can modify significantly the dynamic behavior of the corresponding deterministic system. Indeed, when they are computed on the latter, the two quantities aforementioned have a discontinuity at the mitigation limit (i.e. the value of the bifurcation parameter under consideration below which the NES acts and above which it no longer acts) revealing an abrupt change of behavior of the coupled system. The paper shows that this typical characteristic of the deterministic system is lost in the presence of stochasticity, the stochastic system becoming smooth at the mitigation limit.

Keywords: Passive vibration control, Non-linear energy sink, Self-sustained oscillations, Stochastic averaging, Stochastic forcing

1. Introduction

The non-linear vibration absorbers known as non-linear energy sinks (NESs) are these days well-known devices used for passive mitigation of unwanted oscillations caused by either external, parametric or self-excitations of a mechanical or acoustical primary structure. In general an NES is defined as a non-linear attachment consisting of a light mass (compared to the total mass of the primary structure), an essentially non-linear spring (most of the time purely cubic) and a viscous linear damper. The dependence between the vibratory amplitude and the oscillating frequency of the NES (because of its strongly non-linear nature) makes it able to resonate at any frequency. After tuning to the primary structure and having absorbed and then dissipated its energy, the NES can detune from the primary structure to avoid the return of energy. This irreversible transfer of vibrational energy from the primary system to the NES is called targeted energy transfert (TET) or energy pumping. In their seminal papers [1, 2] Gendelman, Vakakis and al. explain the TET phenomenon by the interaction between two non-linear modes of vibrations of the system producing a 1:1 resonance capture. Reviews of these concepts can be found in [3] and more recently in [4].

Using an NES to alleviate or even suppress limit cycle oscillations (LCOs) resulting from dynamic instabilities has been extensively studied in the literature in a deterministic framework. Mitigation of LCOs of the Van der Pol oscillator has been studied numerically by Lee and al. in their seminal paper [5] and then theoretically by Gendelman and Bar [6]. This latter work has been extended to a Van der Pol-Duffing oscillator coupled to one NES by Domany and Gendelman [7]. A number of works focused on the problem of mitigation, using one or several NESs, of LCOs due to flutter instabilities in aircraft wings. This problem has been first studied both numerically and experimentally, again by Lee. and al. [8, 9, 10]. The theoretical prediction of observed operating regimes has been performed by means of multiple time scales approaches [11, 12] and improved more recently using the center manifold reduction technique [13]. Also in the context of self-oscillations induced by fluid-structure interactions, the mitigation of vortex-induced vibrations caused by the non-linear interaction of a laminar flow and a rigid circular cylinder has been first investigated by Tumkur

*Corresponding author

Email address: baptiste.bergeot@insa-cvl.fr (Baptiste Bergeot)

and al. [14] constructing a two-DOFs reduced-order model and validating it by means of a comparison with a finite-element model. An improved and experimentally validated reduced-order model has been proposed by Dai and al. [15]. On the same issue, a recent theoretical work [16] (i) explains the global dynamics of the system by means a three-DOFs reduced-order model coupling fluid-structure interaction framework with the NES attachment and (ii) identifies, through a parametric study, the optimal operational parameter ranges for an efficient NES design. Concerning aeronautics, the use of NESs to control helicopter ground resonance instability has been studied in [17, 18]. The use of several NESs to alleviate self-sustained oscillations has been analytically studied by Bergeot and Bellizzi in two papers. First, the use of several parallel NESs attached to a Van der Pol oscillator has been analyzed in [19]. Then, the prediction of the dynamic behavior of a multi-DOFs mechanical system with only one unstable mode and coupled to a set of NESs has been proposed in [20] with an application to flutter instability of an airplane wing model. Finally, the possibility of mitigating self-sustained oscillations of a linear friction system having two unstable modes has been studied by Bergeot and al. [21] by means of a sophisticated multiple time scales analysis allowing the understanding of the phenomena underlying the appearance of the many possible regimes of the system.

Many engineering applications, especially in the context of fluid-structure interaction and aeronautics, involve stochasticity which can have an important influence on the deterministic dynamics. Although that often leads to a better understanding of the dynamics of a mechanical system under more realistic conditions, there are very few papers that study the TET mechanisms taking into account stochasticity. The polynomial chaos approach has been used by Gourdon and Lamarque [22] to analyze the NESs behavior during instationary regimes in a two-DOFs academic system. The goal was to verify the robustness of the TET mechanism when the model has uncertain parameters. In the same vein, Cataldo and al. [23] used the Monte Carlo method to study the energy pumping robustness considering the uncertainties of the parameters of a linear primary structure coupled to an NES. The design optimization of parallel NESs taking into account uncertainties has been performed in [24]. In the context of limit cycles mitigation, Pidaparthi and Missoum [25] performed optimization under uncertainties of an NES used to alleviate limit cycles created by aeroelastic instability in an aircraft wing. Snoun and al. [26] used a multi-element generalized polynomial chaos based method to predict the dynamic behavior of an uncertain friction system coupled to two non-linear energy sinks. A robust method was proposed to optimize non-linear energy sinks (NES) in the same model in [27].

In the previous cited works, the stochasticity comes from parametric uncertainties considering that parameters values cannot be known exactly. This approach, however, assumes that for a given realization of the process the parameters are constant. Each realization is therefore deterministic. Another approach consists in investigating the TET taking into account a stochastic time dependent forcing. Even fewer works consider this approach. Schmidt and Lamarque [28] studied a linear one-DOF primary structure coupled to one NES in presence of a white noise forcing by solving numerically the Fokker-Planck equation associated with the stochastic equations of motion of the system. Starosvetsky and Gendelman [29] showed, using numerical simulations, that an NES can produce complete elimination of undesired response of a linear one-DOF system subject to a randomly modulated and narrow-band excitation. A TET problem from a linear medium to a non-linear attachment is studied in the presence of stochasticity by Sapsis and al. [30]. Using a stochastic averaging method, the authors determine the equation of the stochastic slow flow dynamics of the system. Numerical integration of the associated Fokker-Planck equation reveals that the optimal TET regimes, predicted in the deterministic case, are preserved and even enhanced because of the interaction between non-linearity and stochasticity.

In the present paper we consider the problem of mitigation of self-sustained oscillations by means of an NES in presence of stochasticity (in the form of a Gaussian white noise forcing) which, to the knowledge of the author, has not been treated in the literature. The problem is studied using the standard stochastic averaging method [31, 32, 33] to compute the slow flow dynamics of a Van der Pol oscillator undergoing a Gaussian white noise forcing and coupled to an NES. Then two quantities are introduced to highlight the special features of the stochastic system, in comparison with the behavior of the deterministic system. These are the *probability of being in a harmless regime* and the *First-Passage Time to reach a harmful regime* which are studied using the Monte Carlo method [34] combined with numerical simulations of the stochastic slow flow.

The paper is organized as follows. In Section 2 the equations of motion of the full-order system under study - i.e. a Van der Pol oscillator forced by a stochastic forcing (Gaussian white noise) and coupled to a purely cubic non-linear energy sink - are derived. The standard stochastic averaging method is used in Section 3 to compute the slow flow dynamics of the full-order system. Section 4 recalls the typical behavior of the deterministic system (in Section 4.1) with the aim of highlighting some special features caused by stochasticity (in Section 4.2). The probability of being in a harmless regime and the First-Passage Time to reach a harmful regime are defined and then investigated by means of the Monte Carlo method in Sections 5 and 6 respectively. Finally, concluding remarks and perspectives are formulated in Section 7.

2. Equations of the model

In this section we derive the equations of motion of the full-order system under study, i.e. a Van der Pol (VdP)

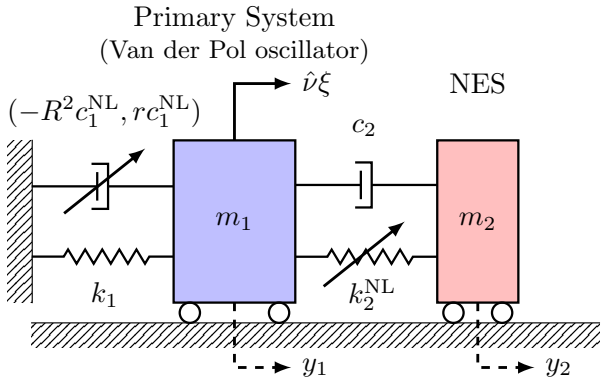

Figure 1: A Van der Pol oscillator (primary system) with stochastic forcing (Gaussian white noise) $\hat{\nu}\xi$ and coupled to an NES.

oscillator - used as an archetypal self-sustained oscillator - forced by a Gaussian white noise and coupled to an ungrounded purely cubic non-linear energy sink (NES). A schematic representation of this system is depicted in Fig. 1. The equations of motion of this system are as follows

$$m_1\frac{\mathrm{d}^2y_1}{\mathrm{d}t^2}+c_1^{\mathrm{NL}}\frac{\mathrm{d}y_1}{\mathrm{d}t}\left(ry_1^2-R^2\right)+k_1y_1+ c_2\left(\frac{\mathrm{d}y_1}{\mathrm{d}t}-\frac{\mathrm{d}y_2}{\mathrm{d}t}\right)+k_2^{\mathrm{NL}}\left(y_1-y_2\right)^3=\hat{\nu}\xi(t) \tag{1a}$$

$$m_2\frac{\mathrm{d}^2y_2}{dt^2}+c_2\left(\frac{\mathrm{d}y_2}{\mathrm{d}t}-\frac{\mathrm{d}y_1}{\mathrm{d}t}\right)+k_2^{\mathrm{NL}}(y_2-y_1)^3=0 \tag{1b}$$

where m_1 and m_2 are the masses of the primary VdP oscillator and of the NES respectively. The parameter k_1 is the linear stiffness of the VdP oscillator and c_1^{NL} and rc_1^{NL} characterize its negative and non-linear dampings respectively. The NES is a purely cubic oscillator characterized by its linear damping coefficient c_2 and non-linear stiffness k_2^{NL}. The term $\xi(t)$ is a unitary idealized white noise process with zero mean, i.e.

$$\mathbb{E}\left[\xi(t)\right]=0 \quad \text{and} \quad \mathbb{E}\left[\xi(t)\xi(t+\tau)\right]=\delta(\tau) \tag{2}$$

where $\hat{\nu}$ is the noise level.

For convenience Eq. (2) is rescaled leading to the following dimensionless system of differential equations

$$\ddot{x}_1+\epsilon\rho\dot{x}\left(rx_1^2-1\right)+x_1+ \epsilon\mu\left(\dot{x}_1-\dot{x}_2\right)+\epsilon\alpha(x_1-x_2)^3=\epsilon\nu\xi(t') \tag{3a}$$

$$\epsilon\ddot{x}_2+\epsilon\mu\left(\dot{x}_2-\dot{x}_1\right)+\epsilon\alpha(x_2-x_1)^3=0 \tag{3b}$$

where $x_i=y_i/R$ $(i=1,2)$, $\omega_1=\sqrt{k_1/m_1}$, $t'=\omega_1 t$, $\dot{\{\}}=d\{\}/dt'$, $\epsilon=m_2/m_1$ is the mass ratio between the NES and the VdP oscillator, $\rho=c_1^{\mathrm{NL}}R^2/(m_2\omega_1)$, $\mu=c_2/(m_2\omega_1)$, $\alpha=k_2^{\mathrm{NL}}R^2/(m_2\omega_1^2)$ and $\nu=\hat{\nu}/(m_2R\omega_1^{3/2})$. In the latter, the exponent 3/2 is obtained recalling that a normalized white noise $\xi(t)$ is defined as the time derivative of the normalized Wiener process $W(t')$ and using the *scaling property of Wiener process* (see [35], Chap. 2) which states that $W(t'/\omega_1)$ and $1/\sqrt{\omega_1}W(t')$ are the same stochastic processes. Therefore, we have

$$\begin{aligned}\xi(t)=\frac{\mathrm{d}W(t)}{\mathrm{d}t}&\sim\omega_1\frac{\mathrm{d}W(\frac{t'}{\omega_1})}{\mathrm{d}t'}\sim\sqrt{\omega_1}\frac{\mathrm{d}W(t')}{\mathrm{d}t'}\\ &=\sqrt{\omega_1}\xi(t')\end{aligned} \tag{4}$$

that explains the expression of parameter ν.

Finally, using the change of variable $u_1=x_1+\epsilon x_2$ and $u_2=x_1-x_2$ the equations of motion (3) become

$$\ddot{u}_1+u_1-\epsilon\left[\rho\dot{u}_1(ru_1^2-1)+u_1-u_2\right]=\epsilon\nu\xi(t') \tag{5a}$$

$$\ddot{u}_2+\mu\dot{u}_2+\alpha u_2^3- \epsilon\left[\rho\dot{u}_1(ru_1^2-1)+u_1-\mu\dot{u}_2-u_2-\alpha u_2^3\right]=\epsilon\nu\xi(t') \tag{5b}$$

in which a first order Taylor expansion around $\epsilon=0$ has been performed assuming a small mass ratio between the NES and the primary oscillator (i.e. $0<\epsilon\ll 1$).

In the next sections, the time t' is denoted by t for the sake of conciseness.

3. The stochastic slow flow dynamics

The standard stochastic averaging method [31, 33], whose general formulation is recalled in Appendix B, is used in this section to obtain the equations governing the stochastic slow flow dynamics of Eq. (5).

TET is due to the interaction between two non-linear modes of the coupled structure [1, 2]. This phenomenon, called a 1:1 resonance capture, occurs at a frequency close to the natural frequency of the primary structure, here the VdP oscillator. It is customary to study the dynamic behavior of the system in the neighborhood of this 1:1 resonance capture. Then, the system is simplified by averaging it over a natural period of the primary structure using the Krylov-Bogolyubov averaged approximation (see e.g. [36]). The resulting averaged dynamics is called slow flow. In general, in the context of NES studies, the complexification-averaging method [37, 3] is used. Here a real amplitude-angle representation (completely equivalent to the latter) is preferred by stating

$$u_1=a_1\cos\left(t+\varphi_1\right) \tag{6a}$$

$$\dot{u}_1=-a_1\sin\left(t+\varphi_1\right) \tag{6b}$$

and

$$u_2=a_2\cos\left(t+\varphi_2\right) \tag{7a}$$

$$\dot{u}_2=-a_2\sin\left(t+\varphi_2\right). \tag{7b}$$

The imposed forms of Eqs. (6b) and (7b) require that

$$\dot{a}_1\cos\phi_1-a_1\dot{\varphi}_1\sin\phi_1=0, \tag{8}$$

and

$$\dot{a}_2\cos\phi_2-a_2\dot{\varphi}_2\sin\phi_2=0, \tag{9}$$

with

$$\phi_1 = t + \varphi_1 \quad \text{and} \quad \phi_2 = t + \varphi_2 \tag{10}$$

that leads to

$$\dot{\varphi}_1 = \frac{\dot{a}_1}{a_1}\frac{\cos\phi_1}{\sin\phi_1}, \quad \dot{a}_1 = a_1\dot{\varphi}_1\frac{\sin\phi_1}{\cos\phi_1}, \tag{11a}$$

$$\dot{\varphi}_2 = \frac{\dot{a}_2}{a_2}\frac{\cos\phi_2}{\sin\phi_2} \quad \text{and} \quad \dot{a}_2 = a_2\dot{\varphi}_2\frac{\sin\phi_2}{\cos\phi_2}. \tag{11b}$$

Then differentiation of Eqs. (6b) and (7b) yields

$$\ddot{u}_1 = -a_1\cos\phi_1 - \dot{a}_1\sin\phi_1 - a_1\dot{\varphi}_1\cos\phi_1. \tag{12}$$

and

$$\ddot{u}_2 = -a_2\cos\phi_2 - \dot{a}_2\sin\phi_2 - a_2\dot{\varphi}_2\cos\phi_2. \tag{13}$$

The substitution of Eqs. (6), (7), (12) and (13) into Eq. (5) and the use of Eq. (11) leads to the following $(2,2)$-fast-slow non-autonomous system of stochastic differential equations

$$\dot{a}_1 = \epsilon f_1(a_1,\varphi_1,a_2,\varphi_2,t) - \epsilon\nu\xi\sin\phi_1 \tag{14a}$$

$$\dot{\varphi}_1 = \epsilon f_2(a_1,\varphi_1,a_2,\varphi_2,t) - \epsilon\nu\xi\frac{\cos\phi_1}{a_1} \tag{14b}$$

$$\dot{a}_2 = f_3(a_1,\varphi_1,a_2,\varphi_2,t,\epsilon) - \epsilon\nu\xi\sin\phi_2 \tag{14c}$$

$$\dot{\varphi}_2 = f_4(a_1,\varphi_1,a_2,\varphi_2,t,\epsilon) - \epsilon\nu\xi\frac{\cos\phi_2}{a_2} \tag{14d}$$

where the expressions of the functions f_1, f_2, f_3 and f_4 are given in Appendix A.

The terms of order $\mathcal{O}(\epsilon)$ are neglected in the equations of the fast variables (i.e. Eqs. (14c) and (14d)), that leads to

$$\dot{a}_1 = \epsilon f_1(a_1,\varphi_1,a_2,\varphi_2,t) - \epsilon\nu\xi\sin\phi_1 \tag{15a}$$

$$\dot{\varphi}_1 = \epsilon f_2(a_1,\varphi_1,a_2,\varphi_2,t) - \epsilon\nu\xi\frac{\cos\phi_1}{a_1} \tag{15b}$$

$$\dot{a}_2 = f_3(a_1,\varphi_1,a_2,\varphi_2,t,0) \tag{15c}$$

$$\dot{\varphi}_2 = f_4(a_1,\varphi_1,a_2,\varphi_2,t,0) \tag{15d}$$

which has a similar form as (B.1) with

$$\begin{aligned}
\mathbf{x} &= (a_1,\varphi_1,a_2,\varphi_2)^T \\
\mathbf{f}(\mathbf{x},t) &= \begin{pmatrix} \epsilon f_1(a_1,\varphi_1,a_2,\varphi_2,t) \\ \epsilon f_2(a_1,\varphi_1,a_2,\varphi_2,t) \\ f_3(a_1,\varphi_1,a_2,\varphi_2,t,0) \\ f_4(a_1,\varphi_1,a_2,\varphi_2,t,0) \end{pmatrix}, \\
\mathbf{g}(\mathbf{x},t) &= \epsilon\nu\begin{pmatrix} -\sin\phi_1 & 0 \\ 0 & -\dfrac{\cos\phi_1}{a_1} \end{pmatrix}, \\
\boldsymbol{\eta} &= (\xi,\xi,\xi,\xi)^T
\end{aligned} \tag{16}$$

where $()^T$ denotes the transpose operator.

Following the standard stochastic averaging method described in Appendix B, the drift vector $\mathbf{m}$ (see Eq. (B.3)) is first computed. The first term corresponds to classical (deterministic) Krylov-Bogolyubov averaging of the vector function $\mathbf{f}$, here over one period equal to 2π. This term is written as follows

$$M^{\text{av}}\{\mathbf{f}\} = \begin{pmatrix} \epsilon\hat{f}_1(a_1,a_2,\varphi) \\ \epsilon\hat{f}_2(a_1,a_2,\varphi) \\ \hat{f}_3(a_1,a_2,\varphi) \\ \hat{f}_4(a_1,a_2,\varphi) \end{pmatrix} \tag{17}$$

where $\varphi = \varphi_1 - \varphi_2$ and

$$\hat{f}_1(a_1,a_2,\varphi) = \frac{1}{8}\left(4a_2\sin(\varphi) - a_1\left(ra_1^2 - 4\right)\rho\right) \tag{18}$$

$$\hat{f}_2(a_1,a_2,\varphi) = \frac{1}{2}\left(\frac{a_2\cos(\varphi)}{a_1} - 1\right) \tag{19}$$

$$\hat{f}_3(a_1,a_2,\varphi) = \frac{1}{8}\left(-4a_2\mu - 4a_1\sin(\varphi)\right) \tag{20}$$

$$\hat{f}_4(a_1,a_2,\varphi) = \frac{3\alpha a_2^3 + 4a_1\cos(\varphi) - 4a_2}{8a_2} \tag{21}$$

Then the second part of the drift vector $\mathbf{m}$ (see again Eq. (B.3)) is determined as

$$\begin{aligned}
&M^{\text{av}}\left\{\int_{-\infty}^{0}\mathbb{E}\left[\left(\frac{\partial(\mathbf{g}\boldsymbol{\eta})}{\partial\mathbf{x}}\right)_t(\mathbf{g}\boldsymbol{\eta})_{t+s}\right]ds\right\} \\
&= \frac{1}{2\pi}\int_{t_0}^{t_0+2\pi}\int_{-\infty}^{0}\mathbb{E}\left[\left(\frac{\partial(\mathbf{g}\boldsymbol{\eta})}{\partial\mathbf{x}}\right)_t(\mathbf{g}\boldsymbol{\eta})_{t+s}\right]dsdt \\
&= \begin{pmatrix} \frac{\epsilon^2\nu^2}{2a_1}\int_{-\infty}^{0}\delta(s)\cos(s)ds \\ 0 \\ 0 \\ 0 \end{pmatrix}
\end{aligned} \tag{22}$$

in which the symbol $\mathbb{E}[]$ has been removed by means of Eq. (2). Because

$$\int_{-\infty}^{0}\delta(s)\cos(s)ds = \frac{1}{2}\int_{-\infty}^{+\infty}\delta(s)\cos(s)ds = \frac{1}{2} \tag{23}$$

the final expression of the drift vector is obtained as

$$\mathbf{m} = \begin{pmatrix} \epsilon\hat{f}_1(a_1,a_2,\varphi) + \dfrac{\epsilon^2\nu^2}{4a_1} \\ \epsilon\hat{f}_2(a_1,a_2,\varphi) \\ \hat{f}_3(a_1,a_2,\varphi) \\ \hat{f}_4(a_1,a_2,\varphi) \end{pmatrix}. \tag{24}$$

The expression of the diffusion matrix $\boldsymbol{\sigma}$ is now deter-

mined from (B.4). First, $\boldsymbol{\sigma}\boldsymbol{\sigma}^T$ is computed as follows

$$\begin{aligned}\boldsymbol{\sigma}\boldsymbol{\sigma}^T &= M^{\text{av}}\left\{\int_{-\infty}^{+\infty}\mathbb{E}\left[(\mathbf{g}\boldsymbol{\eta})_t(\mathbf{g}\boldsymbol{\eta})_{t+s}^T\right]ds\right\}\\ &= \frac{1}{2\pi}\int_{t_0}^{t_0+2\pi}\int_{-\infty}^{+\infty}\mathbb{E}\left[(\mathbf{g}\boldsymbol{\eta})_t(\mathbf{g}\boldsymbol{\eta})_{t+s}^T\right]dsdt\\ &= \epsilon^2\nu^2\int_{-\infty}^{+\infty}\begin{pmatrix}\frac{\delta(s)\cos(s)}{2} & -\frac{\delta(s)\sin(s)}{2a_1}\\ \frac{\delta(s)\sin(s)}{2a_1} & \frac{\delta(s)\cos(s)}{2a_1^2}\end{pmatrix}ds\\ &= \epsilon^2\nu^2\begin{pmatrix}\frac{1}{2} & 0 & 0 & 0\\ 0 & \frac{1}{2a_1^2} & 0 & 0\\ 0 & 0 & 0 & 0\\ 0 & 0 & 0 & 0\end{pmatrix}.\end{aligned} \tag{25}$$

Therefore, from (25) a possible solution of (B.4) is

$$\boldsymbol{\sigma} = \epsilon\nu\begin{pmatrix}\frac{1}{\sqrt{2}} & 0 & 0 & 0\\ 0 & \frac{1}{a_1\sqrt{2}} & 0 & 0\\ 0 & 0 & 0 & 0\\ 0 & 0 & 0 & 0\end{pmatrix}. \tag{26}$$

According to (B.2) the equations governing the stochastic slow dynamics of (5) are

$$\dot{a}_1 = \epsilon\hat{f}_1(a_1,a_2,\varphi) + \frac{\epsilon^2\nu^2}{4a_1} + \frac{\epsilon\nu}{\sqrt{2}}\xi(t) \tag{27a}$$
$$\dot{\varphi}_1 = \epsilon\hat{f}_2(a_1,a_2,\varphi) + \frac{\epsilon\nu}{a_1\sqrt{2}}\xi(t) \tag{27b}$$
$$\dot{a}_2 = \hat{f}_3(a_1,a_2,\varphi) \tag{27c}$$
$$\dot{\varphi}_2 = \hat{f}_4(a_1,a_2,\varphi) \tag{27d}$$

The final form of the stochastic slow flow is obtained by combining Eqs. (27b) and (27d), that leads to

$$\dot{a}_1 = \epsilon f(a_1,a_2,\varphi) + \epsilon\sigma\xi(t) \tag{28a}$$
$$\dot{a}_2 = g_1(a_1,a_2,\varphi) \tag{28b}$$
$$\dot{\varphi} = g_2(a_1,a_2,\varphi) \tag{28c}$$

where $f = \hat{f}_1$, $g_1 = \hat{f}_3$, $\sigma = \frac{\nu}{\sqrt{2}}$ and the term $\frac{\epsilon^2\nu^2}{4a_1}$ (of order $\mathcal{O}(\epsilon^2)$) has been neglected in Eq. (28a). The difference between Eqs. (27b) and (27d) should yield $\epsilon\hat{f}_2(a_1,a_2,\varphi) + \frac{\epsilon\nu}{a_1\sqrt{2}}\xi - \hat{f}_4(a_1,a_2,\varphi)$ as the right-hand side of Eq. (28c). However, the terms of order $\mathcal{O}(\epsilon)$ are neglected, one has therefore only $g_2 = -\hat{f}_4(a_1,a_2,\varphi)$ remains. Equation (28) appears as a stochastic $(2,1)$-fast-slow system where a_2 and φ are the fast variables and a_1 is the slow variable on which the noise acts.

A key mathematical tool for the description of a fast-slow system such as Eq. (28) is its critical manifold. The latter is defined in this section. First, the slow flow (28) is written with respect to the slow time $\tau = \epsilon t$ as follows

$$a_1' = f(a_1,a_2,\varphi) + \sqrt{\epsilon}\sigma\xi(\tau) \tag{29a}$$
$$\epsilon a_2' = g_1(a_1,a_2,\varphi) \tag{29b}$$
$$\epsilon\varphi' = g_2(a_1,a_2,\varphi) \tag{29c}$$

where $(.)'$ denotes the derivative with respect to the slow time τ. Again the scaling property of the Wiener process has been used, i.e. $\xi(t) = \sqrt{\epsilon}\xi(\tau)$. Considering $\epsilon = 0$ respectively in Eqs. (28) and (29) yields the *slow subsystem*

$$a_1' = f(a_1,a_2,\varphi) \tag{30a}$$
$$0 = g_1(a_1,a_2,\varphi) \tag{30b}$$
$$0 = g_2(a_1,a_2,\varphi), \tag{30c}$$

which is a differential-algebraic equation, and the *fast subsystem*

$$\dot{a}_1 = 0 \tag{31a}$$
$$\dot{a}_2 = g_1(a_1,a_2,\varphi) \tag{31b}$$
$$\dot{\varphi} = g_2(a_1,a_2,\varphi). \tag{31c}$$

The critical manifold of the slow flow is the solution of the algebraic part of Eq. (30) and it is expressed as follows

$$\mathcal{M}_0 = \Big\{(a_1,a_2,\varphi)\in\mathbb{R}^{+^2}\times[-\pi,\pi]\ \Big|\ g_1(a_1,a_2,\varphi) = 0 \text{ and } g_2(a_1,a_2,\varphi) = 0\Big\}. \tag{32}$$

Note that because of the assumptions made (i.e. a noise which acts only on the primary structure with a level of the order $\mathcal{O}(\epsilon)$), the effect of the noise on the fast variables a_2 and φ has been neglected. Consequently both slow and fast subsystems are deterministic. This has two major consequences. First, the critical manifold is deterministic too ans it can therefore be obtained with the usual approach (the classical analysis of the deterministic slow flow including the computation of the critical manifold is recalled in Appendix C). Then, it means that the role of the noise cannot be investigated within the zeroth-order approximation, i.e. within the limit case in which the perturbation parameter ϵ is equal to zero, as it is usually done in the context of NES studies.

4. Problem statement and preliminary results

In this section we first recall in Section 4.1 how the deterministic system behaves using both numerical simulations of the deterministic slow flow (i.e. Eq. (29) with $\sigma = 0$) and the classical analytical results presented in Appendix C. Then, in Section 4.2, the comparison with numerical integration of the stochastic slow flow (29) (using the function `ItoProcess` of Mathematica software [38]) allows us to highlight the influence of noise on the system behavior.

4.1. Reminder of the deterministic behavior of the system

The slow-fast nature of the slow flow implies that it evolves at two time scales: the slow time scale τ in which the slow flow is on the critical manifold and approximatively described by the slow subsystem (30) and the fast time scale t in which the slow flow is outside the critical manifold and described by the fast subsystem (31). The particular S-shape of the critical manifold (see Fig. C.9) together with the stability analysis of the fixed points of the slow flow allows to explain and predict its different responses and consequently those of the full-order system. Four scenarios are possible and in previous works by the authors [19, 20] these responses are classified into two categories called *harmless situations* and *harmful situations*. In harmless situations, the NES acts, resulting in three possible responses. The first scenario is called *Complete suppression*. In this case the trivial fixed point of the slow flow is stable and then reached. This is a linear effect of the NES and, in the context of non-linear vibrations absorption, the complete suppression is not the desired effect. The second possible regime is called *mitigation through periodic responses (PRs)*. This corresponds to the situation in which a nontrivial stable fixed point of the slow flow is reached leading to a periodic regime for the initial full-order system. The last harmless situations correspond to *mitigation through Strongly Modulated Responses (SMRs)*. SMRs are quasi-periodic regimes (amplitude and phase modulated) of the full-order system corresponding to relaxations oscillations of the slow flow. There is only one type of harmful situations for which the NES is not able to produce small amplitude responses. In this case, a limit cycle with an amplitude close to that of the Van der Pol oscillator alone is observed.

In general, the transition from harmless to harmful situations corresponds to the transition from an SMR to a no mitigation regime. This transition is illustrated in Fig. 2: Figs. 2(a) and 2(c) show a relaxations oscillation scenario and Figs. 2(b) and 2(d) show a no mitigation scenario. The top figures depict the times series of the amplitude a_1 and a_2 at the slow time scale τ and the bottom figures depict the comparison between the trajectory of the slow flow and the critical manifold (32) in the (a_2, a_1)-plane. In the latter (see Figs. 2(c) and 2(d)), in both relaxation oscillations and no mitigation scenarios, from an initial condition near zero and outside the critical manifold, the trajectory of the slow flow evolves rapidly and almost horizontally to the left attracting branch of $\mathcal{M}_0$. During this fast epoch the slow flow dynamics is approximatively described by the fast subsystem (31). Then, the slow flow evolves slowly close to this branch. During this slow epoch the slow flow dynamics is now approximatively described by the slow subsystem (30). If the trajectory does not meet a stable fixed point[1], the trajectory goes toward the left fold point $(a_2^{\mathrm{LF}}, a_1^{\mathrm{LF}})$ at which $\mathcal{M}_0$ becomes repelling (see Eqs. (C.2), (C.4) and (C.5)).

Remark. When the full-order system passes from a PR to an SMR (i.e. when the slow flow passes from a reached stable fixed point to stable relaxation oscillations) *folded singularities* can appear. The latter are points for which fold and fixed points of the slow flow coincide and are hints of particular solutions of fast-slow systems, called *canards* (see e.g. [39] for rigorous mathematical definitions of these concepts). In general, canard solutions appear for a very small range of the bifurcation parameter and are not investigated in this paper.

The zeroth-order approximation assumes that the left fold point is actually reached. However numerical simulations show that when approaching the left fold point the trajectory deviates slightly from the critical manifold (this behavior is analytically described in [13]). Then the slow flow undergoes a fast and nearly horizontal jump to the right attracting part of $\mathcal{M}_0$ on a point called *arrival point*[2]. This is where the two scenarios differ. In the case of relaxation oscillations the largest unstable fixed point of the slow flow (depicted by a green bullet on the figures) is above the arrival point and prevents the trajectory from reaching the stable fixed point located higher on the critical manifold. This fixed point is not depicted on Figs. 2(c) and 2(d), its coordinates in the (a_2, a_1)-plane are $(1.51, 6.28)$. If this fixed point is reached the system undergoes a no mitigation regime. This is what happens when the largest unstable fixed point of the slow flow is below the arrival point (see Fig. 2(d)). The end of the scenario of relaxation oscillations is as follows (see Fig. 2(c)): from the arrival point a second slow epoch occurs in which the trajectory goes toward the right fold point $(a_2^{\mathrm{RF}}, a_1^{\mathrm{RF}})$. A second nearly horizontal jump occurs and the trajectory returns to the left attracting part of $\mathcal{M}_0$. A third slow epoch on $\mathcal{M}_0$ towards $(a_2^{\mathrm{LF}}, a_1^{\mathrm{LF}})$ is observed, and so on.

Then the **mitigation limit**, defined below, is introduced to quantify the NES efficiency.

Definition 4.1 (Mitigation limit)**.** Considering a set of initial conditions (for the slow flow) as a small perturbation of the trivial solution, the **mitigation limit** is defined as the value of the bifurcation parameter ρ which separates harmless situations from the harmful situation.

For the set of parameters used in Fig. 2, using numerical simulations of the slow flow we find a mitigation limit equal to $\rho_{\mathrm{ml}} = 1.9$. The numerical simulations of the deterministic full-order system (i.e. Eq. (5) with $\nu = 0$) give $\rho_{\mathrm{ml}} = 1.86$.

In the deterministic case the mitigation limit can be predicted analytically by means of a slow-fast partition of the slow flow dynamics [6, 13].

[1] If this is the case the trajectory stops and a mitigation through a PR is observed.

[2] The zeroth-order approximation supposes that the arrival point is $(a_2^{\mathrm{U}}, a_1^{\mathrm{LF}})$ (see Eq. (C.6) and Fig. C.9). In fact, the arrival point is slightly higher on the critical manifold [13].

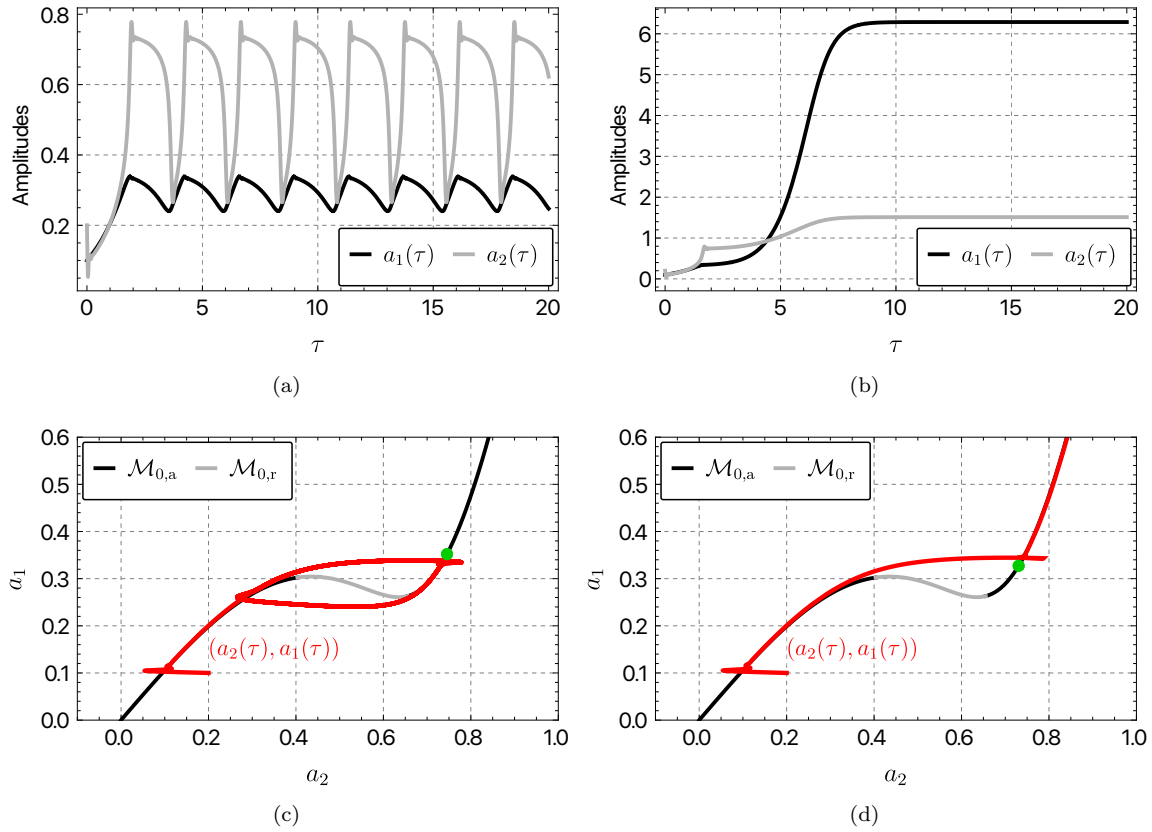

Figure 2: Transition from relaxation oscillations scenario (Figs. 2(a) and 2(c)) to no mitigation scenario (Figs. 2(b) and 2(d)). The top figures show the times series (obtained from numerical integration of the deterministic slow flow, i.e. Eq. (29) with $\sigma = 0$) of the amplitudes a_1 (solid black lines) and a_2 (solid gray lines) at the slow time scale τ and the bottom figures show the comparison between the trajectory of the slow flow (solid red lines) and the critical manifold (32) in the (a_2, a_1)-plane. The following set of parameters is used: $r = 0.1$, $\epsilon = 0.01$, $\mu = 0.4$, $\alpha = 3$ and $\rho = 1.8$ in (a) and (c) and $\rho = 2$ in (b) and (d).

4.2. Influence of noise on the system behavior

In this section we highlight how noise affects the system behavior and more precisely how it influences the mitigation limit. For this purpose, we show in Fig. 3 the result of the numerical simulations of the stochastic slow flow (29) using the same parameters as in Section 4.1 with, in addition, $\sigma = 0.5$.

In Figs. 3(a), 3(b), 3(e) and 3(f), two samples are shown for $\rho = 1.8$, a value of the bifurcation parameter smaller than the mitigation limit $\rho_{\mathrm{ml}} = 1.9$. Therefore, in the deterministic case, we observe persistent relaxation oscillations (see Figs. 2(a) and 2(c)). In the deterministic case all cycles of relaxation oscillations are equivalent, whereas in the stochastic case the trajectory of the slow flow is, due to the presence of noise, slightly different at each cycle. The two samples depicted in the figures show that persistent relaxation oscillations can still occur. We can see in Fig. 3(e) that over the 8 cycles observed (see Fig. 3(a)), 7 correspond to a scenario similar to the deterministic case (i.e. the arrival point on the right attracting part of of $\mathcal{M}_0$ is below the largest fixed point of the deterministic slow flow). There is however one cycle where the arrival point is above the fixed point and where the trajectory still descends towards the right fold point instead of ascending towards the stable fixed point. For the second sample (see Figs. 3(b) and 3(f)) it is the contrary. Indeed, we observe one and a half cycle, and halfway through the second we see that even if the arrival point is below the unstable fixed point the trajectory ascends towards the stable fixed point and a no mitigation regime finally occurs.

In Figs. 3(c), 3(d), 3(g) and 3(h) two samples are depicted for $\rho = 2$, a value of the bifurcation parameter larger than the mitigation limit $\rho_{\mathrm{ml}} = 1.9$. Consequently, in the deterministic case, we observe a no mitigation regime (see Figs. 2(b) and 2(d)). The first sample (see Figs. 3(c) and 3(g)) shows that during the first cycle, the noise prevents the trajectory from reaching the stable fixed point corresponding to the no mitigation regime, which is finally reached in the second cycle. In this example, at each cycle the regime actually reached can be deduced in a similar way as in deterministic case comparing the relative position of the arrival point and the largest unstable fixed point. However, as in the previous example for $\rho = 1.8$, this reasoning can be contradicted in a positive way (favoring the relaxation oscillations) or in a negative way (favoring the no mitigation regimes). For example, in the second

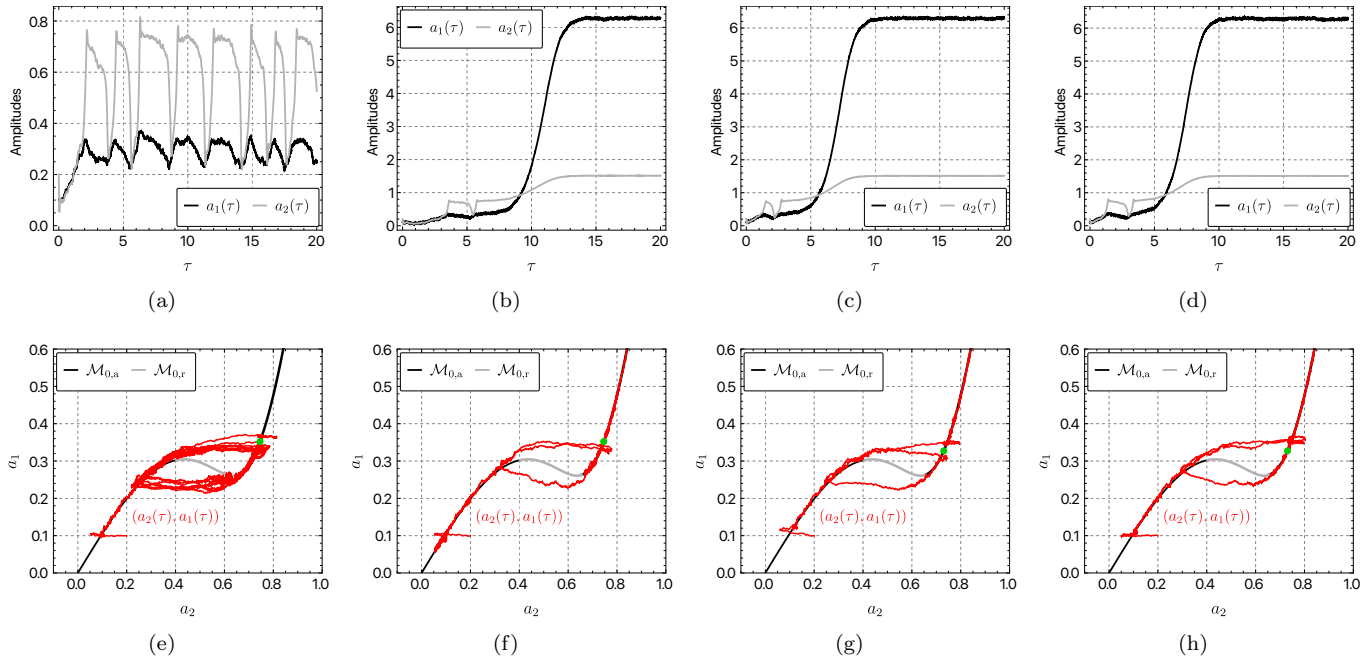

Figure 3: Numerical simulations of the stochastic slow flow (29) using the same parameters as in Section 4.1 with, in addition, $\sigma = 0.5$. In Figs. 3(a), 3(b), 3(e) and 3(f) (resp. Figs. 3(c), 3(d), 3(g) and 3(h)) two samples are shown for $\rho = 1.8$ (resp. $\rho = 2$). Figures 3(a) to 3(d) show the time series of a_1 (black lines) and a_2 (gray lines) and Figs. 3(e) to 3(h) show the trajectory (red lines) of the slow flow and the critical manifold $\mathcal{M}_0$ (gray and black lines) in the (a_1, a_2)-plane.

sample (see Figs. 3(d) and 3(h)) we can see that during the first cycle, the arrival point is above the largest fixed point but the trajectory still descends towards the right fold point.

The previous preliminary results confirm that the effect of the noise cannot be only studied with the zeroth-order approximation. Indeed, as in the deterministic case the trajectory of the slow flow dynamics moves away from the critical manifold when it passes near the left fold point [13, 40]. The zeroth-order approximation [6] assumed that the trajectory goes along the critical manifold and reaches the left jump before jumping to the right attractive part of the critical manifold. However, in the deterministic case the zeroth-order approximation is sufficient to describe the slow epochs of the slow flow except in the neighborhood of the left fold points. Combining the center manifold reduction technique to describe the the slow flow dynamics near the left fold point and the zeroth-order approximation elsewhere, and following the reasoning described in Section 4.1, allows an accurate prediction of the mitigation limit [13]. Here, in the stochastic case, the latter reasoning can be wrong to predict the actual regime and therefore the mitigation limit. That means that the noise acts at the slow time scale in contradiction with the zeroth-order approximation (see Eqs. (30) and (31) and the comments below).

In the next sections the Monte Carlo method is used to study the effect of the noise on the dynamic behavior of the system in a more systematic way. To achieve that, two quantities are introduced: (i) the *probability of being in a harmless regime* and (ii) the *First-Passage Time to reach a harmful regimes*.

5. Probability of being in a harmless regime

Definition 5.1 (The probability of being in a harmless regime)**.** The probability of being in a harmless regime (PBHR), denoted by $p_{\mathrm{h},n}$, is, as its name suggests, the probability for the system of being in a harmless regime after a given number n of full cycles of relaxation oscillations.

For instance, in the case shown in Figs. 3(b) and 3(f), the trajectory of the slow flow ascends towards the stable fixed point (to reach a no mitigation regime) halfway through the second cycle of relaxation oscillations, therefore after one full cycle. In practice, $p_{\mathrm{h},n}$ is computed as the proportion of samples for which we observe at least $n+1$ consecutive full cycles of relaxation oscillations from the beginning of the sample. For example, if 4 samples are computed and we observe: 1 full cycle in the first sample (as in Figs. 3(b) to 3(d)), 0 full cycle in the second sample (as in the deterministic case shown in Fig. 2(b)) and 3 and 2 full cycles in the third and fourth samples respectively, then the corresponding PBHR are $p_{\mathrm{h},0} = \frac{3}{4}$, $p_{\mathrm{h},1} = \frac{2}{4}$, $p_{\mathrm{h},2} = \frac{1}{4}$ and $p_{\mathrm{h},n} = 0$ for $n \geq 3$.

Figure 4 shows the PBHR $p_{\mathrm{h},0}$ obtained from 1000 samples of the slow flow (29) and 1000 samples of the full-order

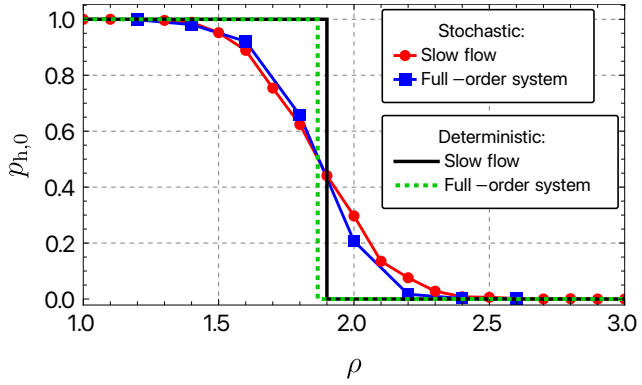

Figure 4: Probabilities $p_{h,0}$ as functions of ρ obtained from 1000 samples of the slow flow (29) (blue squares) and 1000 samples of the full order system (14) (red bullets) and for several values of the bifurcation parameter ρ. The deterministic cases (green dashed line for the slow flow and black line for the full-order system) are also represented. The same parameters as in Section 4.1 are used with, in addition, $\sigma = 0.5$.

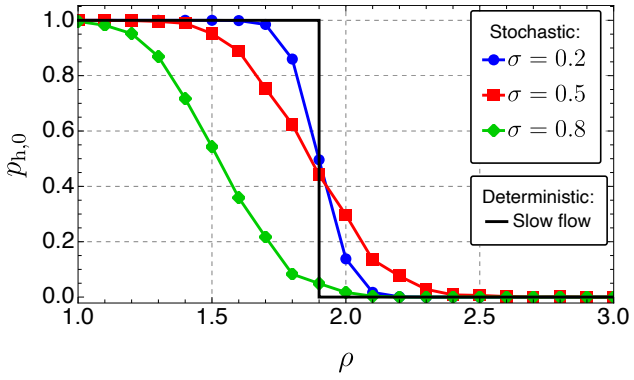

Figure 5: Probabilities $p_{h,0}$ as functions of ρ for three different values of the noise level, i.e. $\sigma = 0.2$ (blue bullets), $\sigma = 0.5$ (red squares) and $\sigma = 0.8$ (green diamonds) and for the same parameters as in Section 4.1.

system (14) and for several values of the bifurcation parameter ρ. The deterministic cases for which $p_{h,0} = 1$ if $\rho < \rho_{ml}$ and $p_{h,0} = 0$ if $\rho > \rho_{ml}$ are also represented (remember that $\rho_{ml} = 1.86$ for the full order system and $\rho_{ml} = 1.9$ for the slow flow). The same parameters as in Section 4.1 are used with, in addition, $\sigma = 0.5$.

First, the figure validates the stochastic averaging procedure. Therefore, in the remaining of the paper, only the slow flow will be used, which allows us to perform the Monte Carlo method with a reasonable computational cost. Indeed with the full-order system, the convergence of the numerical results is obtained with a very small time step, which is highly expensive in terms of computing time.

Then we can see that the step shape observed in the deterministic case, turns into an error function shape in the stochastic case, with $p_{h,0}$ tending to 1 when $\rho \ll \rho_{ml}$ and to 0 when $\rho \gg \rho_{ml}$.

Figure 5 plots $p_{h,0}$ for three different values of the noise level, i.e. $\sigma = 0.2$, $\sigma = 0.5$ and $\sigma = 0.8$. As expected, the

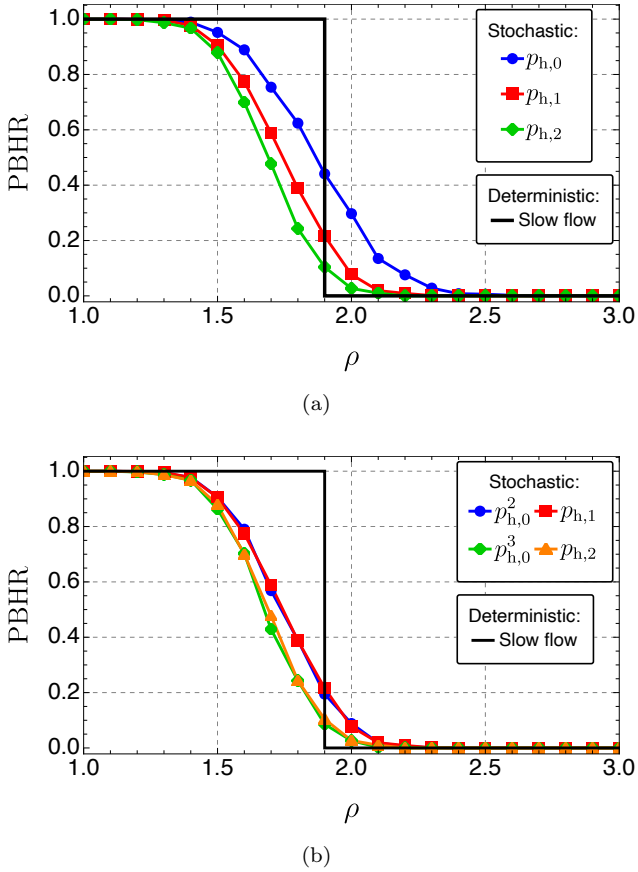

Figure 6: (a) Comparison between $p_{h,0}$ (blue bullets), $p_{h,1}$ (red squares) and $p_{h,2}$ (green diamonds) as functions of the bifurcation parameter ρ. (b) Comparison between $p_{h,0}^2$ (blue bullets), $p_{h,1}$ (red squares), and comparison between $p_{h,0}^3$ (green diamonds) and $p_{h,2}$ (orange triangles). In each figure the deterministic cases (black line) is also represented. The same parameters as in Section 4.1 are used with, in addition, $\sigma = 0.5$.

lower the noise level is, the closer of the deterministic case the system behavior is.

Finally, in Figure 6 we can see the comparison between $p_{h,0}$, $p_{h,1}$ and $p_{h,2}$. First, as expected, we have $p_{h,2} < p_{h,1} < p_{h,0}$ (see Fig. 6(a)). Then, we observe that $p_{h,1} \approx p_{h,0}^2$ and $p_{h,2} \approx p_{h,0}^3 \approx p_{h,0}p_{h,1}$ (see Fig. 6(b)). From these numerical results (and others not shown here) the following generalization is proposed:

$$p_{h,n} \approx \prod_{i=0}^{n-1} p_{h,i} \approx p_{h,0}^{n+1}. \tag{33}$$

This result highlights that at each cycle of relaxation oscillations the probability of being in a harmless regime is independent of the past trajectory of the system (we verified that this also true for the full-order system) and it is equal to $p_{h,0}$.

The PBHR quantifies, in terms of probability, one of the results previously obtained in Section 4.2, namely the fact that no mitigation (resp. mitigation) regimes may occur even if the $\rho < \rho_{ml}$ (resp. $\rho > \rho_{ml}$). It is interesting

to know the probability to be in a harmless regime after a given number of cycles of relaxation oscillations as the value of $p_{\mathrm{h},n}$ tells us. However, the time spent in a harmless regime, i.e. the time the system is safe, is also interesting from an engineering point of view. This is quantified in the next section by computing the *First-Passage Time Density to reach a harmful regime*.

6. First-Passage Time to reach a harmful regime

Let us denote by $(a_1^e, a_2^e, \varphi^e)$ the coordinates of the largest stable fixed point of the deterministic slow flow. Remember that if the trajectory of the slow flow reaches the fixed point the system is in a no mitigation (i.e. harmful) regime (see Section 4.1). Then, we choose that the system is safe as long as $a_1 < a_1^{\mathrm{th}} = 0.5a_1^e$. This choice is arbitrary, it may change depending of the unstable primary structure studied. Next, the First-Passage Time to reach a harmful regime is defined below.

Definition 6.1 (First-Passage Time to reach a harmful regime)**.** If the process starts at $a_1(0) = a_{1,0}$, the first time it reaches the value of the threshold a_1^{th} is called the First-Passage Time to reach a Harmful Regime (FPTHR) and it is denoted by T.

At the slow time scale τ and from the previous definition, the probability $\Pr(\tau < T)$ that $\tau < T$ is the probability $\Pr\left(a_1 < a_1^{\mathrm{th}}\right)$ that $a_1 < a_1^{\mathrm{th}}$. Therefore, one also has

$$\Pr(T < \tau) = \Pr\left(a_1 > a_1^{\mathrm{th}}\right) := P(\tau). \tag{34}$$

Consequently, the probability that the FPTHR T is between the actuel time τ and $\tau + d\tau$ is $R(\tau)d\tau$ where

$$R(\tau) = \frac{dP(\tau)}{d\tau} \tag{35}$$

is the First-Passage Time to reach a Harmful Regime Density (FPTHRD).

The Mean First-Passage Time to reach a Harmful Regime (MFPTHR) denoted by $\mathbb{E}[T]$ is also defined as

$$\mathbb{E}[T] = \int_0^\infty \tau R(\tau) d\tau. \tag{36}$$

In practice, 2000 samples of Eq. (29) are computed. On each sample, the FPTHR is measured as the first value of the time τ for which $a_1(\tau) > a_1^{\mathrm{th}}$. We obtain therefore a list of 2000 values the FPTHR and from it $R(\tau)$, $P(\tau)$ (as histograms) and $\mathbb{E}[T]$ are evaluated.

The Deterministic Passage Time to reach a Harmful Regime (DPTHR), denoted by T_{det}, is defined as the first time $a_1(\tau)$, obtained from the numerical integration of Eq. (29) for $\sigma = 0$ and $a_1(0) = a_{1,0}$, reaches the threshold a_1^{th}. For given initial conditions, T_{det} has a unique finite value if $\rho > \rho_{\mathrm{ml}}$ and tends to infinity if $\rho < \rho_{\mathrm{ml}}$ (i.e. the deterministic system never reaches the threshold a_1^{th}).

Finally, for comparison purposes, a characteristic time is needed. We choose the time, denoted by T_{LF}, at which the deterministic system reaches the neighborhood of the left fold point of the critical manifold (i.e. when $a_1(\tau) = a_1^{\mathrm{LF}}$, obtained from the numerical integration of Eq. (29) for $\sigma = 0$ and $a_1(0) = a_{1,0}$, reaches a_1^{LF}).

Examples of histograms representing $R(\tau)$ and $P(\tau)$ are shown in Fig. 8 (on the left and the right respectively). The same parameters are used as in Section 4.2 with $\rho = 1.8 < \rho_{\mathrm{ml}}$ (see Figs. 7(a) and 7(b)) and $\rho = 2 > \rho_{\mathrm{ml}}$ (see Figs. 7(c) and 7(d)). Vertical lines of equations $\tau = T_{\mathrm{det}}$, $\tau = T_{\mathrm{LF}}$ and $\tau = \mathbb{E}[T]$ are also represented. In Figs. 7(a) and 7(b) the deterministic system is in a mitigation regime and in theory $T_{\mathrm{det}} \to +\infty$. In practice it is equal to the final time of the numerical simulation, here the final time is $\tau = 140$ which outside the frame of the figures. The numerical values of the important times are $T_{\mathrm{det}} = 60$, $T_{\mathrm{LF}} = 3.85$ and $\mathbb{E}[T] = 12$ for $\rho = 1.8$ and $T_{\mathrm{det}} = 7.86$, $T_{\mathrm{LF}} = 3.37$ and $\mathbb{E}[T] = 8.11$ for $\rho = 2$.

We can see in Figs. 7(a) and 7(b) that even if $\rho < \rho_{\mathrm{ml}}$ (i.e. the corresponding deterministic system undergoes a harmless regime), it is almost certain that if we wait for a sufficiently long time the threshold a_1^{th} will be reached. Even for relatively short times (approximately 2 to 4 times T_{LF}) the probability of reaching the threshold is not negligible. To complete the information given in Fig. 7, the values of $P(6)$, $P(10)$ and $P(14)$ for $\rho = 1.7, 1.6, \ldots, 2.4$ are given in Table 1. For example (see Fig. 7(b) and Table 1), we have $P(10) = 0.433$, i.e. if $\tau = 10$ we have a 43.3% chance that the threshold has already been reached. Not surprisingly, for a given value of ρ, the larger the time τ is, the larger $P(\tau)$ becomes; for a given value of τ, the larger ρ is, the larger $P(\tau)$ becomes again. Moreover, these results (those shown in Figs. 7(a) and 7(c)) show that the most likely value is not the deterministic value $\tau = T_{\mathrm{det}}$ which is very close to the mean time $\mathbb{E}[T]$ (see Fig. 7(c)). Contrary to the deterministic case, in the stochastic case we do not see any qualitative difference between the results obtained for $\rho = 1.8$ and those obtained for $\rho = 2$.

The latter observation is even more highlighted in Fig. 8 which compares T_{det}, $\mathbb{E}[T]$ and $\mathbb{E}[T] \pm \sqrt{\mathbb{V}[T]}$ where $\sqrt{\mathbb{V}[T]}$ is the standard deviation of the FPTHR with

$$\mathbb{V}[T] = \mathbb{E}\left[T^2\right] - \mathbb{E}[T]^2 \tag{37}$$

the variance. Indeed, we can see a discontinuity in the graph of T_{det} at $\rho = \rho_{\mathrm{ml}}$ which does not appear in the graphs of $\mathbb{E}[T]$ and $\mathbb{E}[T] \pm \sqrt{\mathbb{V}[T]}$. Again, note that the constant value of the DPTHR, i.e. $T_{\mathrm{det}} = 140$ for $\rho < \rho_{\mathrm{ml}}$, is a numerical artefact. Indeed, when the deterministic system is in a mitigation regimes (here relaxation oscillations of the slow flow) we have $T_{\mathrm{det}} \to +\infty$ in theory. In practice, T_{det} is detected as the final time of the numerical integration which is here $\tau = 140$. Both mean and standard deviation increase when ρ decreases, moving away from the deterministic mitigation limit ρ_{ml}. Finally, we can see again that when $\rho > \rho_{\mathrm{ml}}$ one has $\mathbb{E}[T] \approx T_{\mathrm{det}}$.

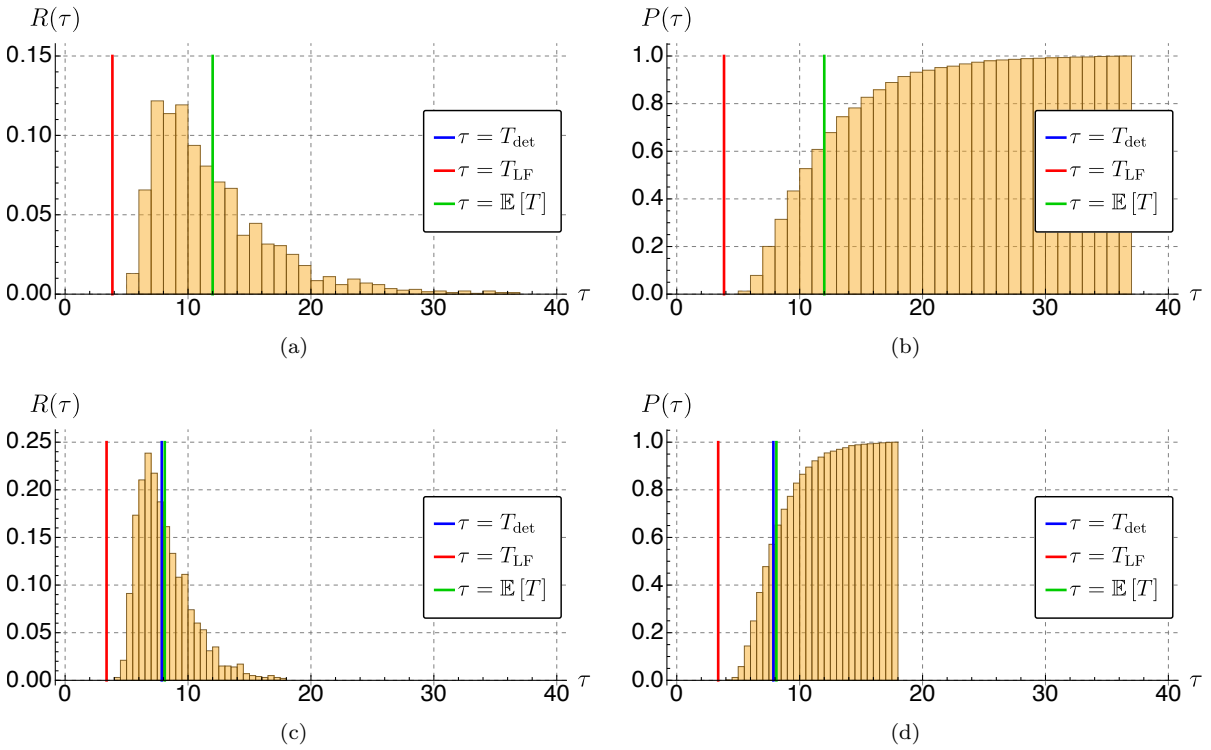

Figure 7: Histograms representing $R(\tau)$ (Figs. 7(a) and 7(c)) and $P(\tau)$ (Figs. 7(b) and 7(d)). Vertical lines of equations $\tau = T_{\text{det}}$ (blue lines), $\tau = T_{\text{LF}}$ (red lines) and $\tau = \mathbb{E}[T]$ (green lines) are also represented. The same parameters as in Section 4.2 are used with $\rho = 1.8 < \rho_{\text{ml}}$ (Figs. 7(a) and 7(b)) and $\rho = 2 > \rho_{\text{ml}}$ (Figs. 7(c) and 7(d)).

Table 1: Values of $P(6)$, $P(10)$ and $P(14)$ for $\rho = 1.7, 1.6, \ldots, 2.4$. The same parameters are used as in Fig. 7.

ρ	1.7	1.8	1.9	2	2.1	2.2	2.3	2.4
$P(6)$	0.003	0.013	0.051	0.144	0.276	0.425	0.563	0.706
$P(10)$	0.219	0.433	0.652	0.828	0.932	0.973	0.985	0.997
$P(14)$	0.5	0.745	0.913	0.977	0.998	1	1	1

In my opinion, what should be retained from the results of this section is the fact that even if the system is supposed to be in an mitigation regime from a deterministic point of view, the amplitude of the self-sustained oscillator can reach a harmful value in a relatively short time with a non-negligible probability.

7. Conclusion

In this paper a Van der Pol oscillator (used as an archetypal self-sustained oscillator) undergoing a white noise forcing and coupled to a non-linear energy sink (NES) has been studied. It was highlighted that the stochastic forcing can modify significantly the dynamic behavior of the corresponding deterministic system. Indeed we showed first, by means of numerical integration of the slow flow dynamics of the system - derived using the standard stochastic averaging method - that the reasoning which allows the theoretical prediction of the system behavior in the deterministic case can be contradicted in presence of stochasticity.

Then the system behavior has been studied in a more systematic way by introducing two quantities: (i) the probability of being in a harmless regime (PBHR), i.e. the probability of obtaining a regime of small amplitude compared to the case without NES; and (ii) the first-passage time to reach a harmful regime (FPTHR), i.e. the time for the system to reach an arbitrary amplitude threshold considered as dangerous if reached by the primary structure. Both quantities have been investigated combining the Monte Carlo approach with numerical integration of the stochastic slow flow dynamics. When they are computed on the corresponding deterministic regime, the PBHR and FPTHR reveal themselves to be discontinuous functions of the bifurcation parameter under consideration. Indeed, at the mitigation limit (i.e. the value of the bifurcation parameter below which the NES acts and above which it no longer acts) the PBHR goes abruptly from 1 (we are sure to be in a mitigation regime) to 0 (we are sure to be in a no mitigation regime), and the FPTHR from infinity (i.e. the deterministic system never reaches the no mitigation regime) to a finite value. We showed

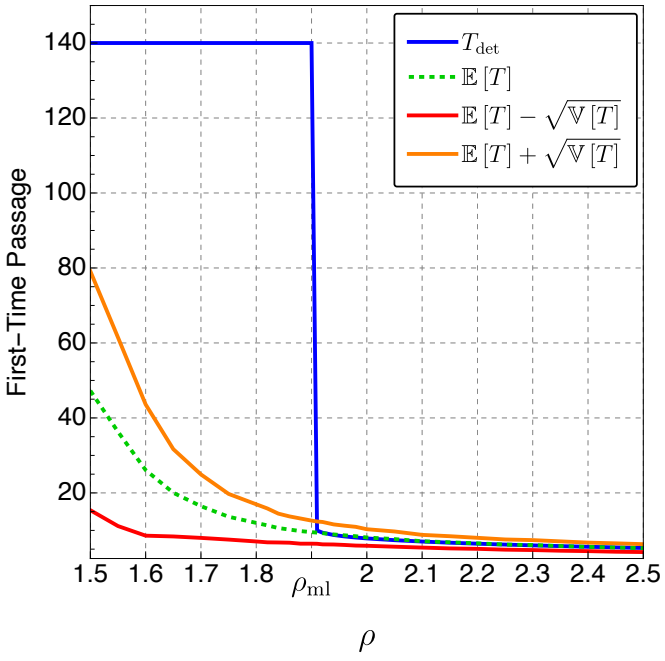

Figure 8: Comparison between T_{det} (blue line), $\mathbb{E}[T]$ (green dashed line), $\mathbb{E}[T] - \sqrt{\mathbb{V}[T]}$ (red line) and $\mathbb{E}[T] + \sqrt{\mathbb{V}[T]}$ (orange line) as function of the bifurcation parameter ρ. The same parameters as in Section 4.2 are used.

that in the stochastic case, both PBHR and FPTHR become smooth at the mitigation limit. This work highlights that taking into account stochasticity allows a better understanding of targeted energy transfer mechanisms in the context of limit cycles mitigation by means of an NES under more realistic conditions than in a deterministic study.

An interesting sequel to this research would be the theoretical analysis of stochastic slow flow inspired by methodologies dedicated to the analysis of noisy slow-fast systems as developed by Berglund and Gentz [41, 42]. This would help to understand the mechanisms underlying the phenomena highlighted in this article.

Appendix A. Expressions of functions

The expressions of the functions f_1, f_2, f_3 and f_4 which appear in Eq. (14) are

$$\begin{aligned} &f_1(a_1,\varphi_1,a_2,\varphi_2,t) = \\ &\frac{1}{2}\Big(a_1 - a_1\rho\cos(2t+2\varphi_1) - a_1\sin(2t+2\varphi_1) \\ &\quad + a_2\sin(2t+\varphi_1+\varphi_2) + a_2\sin(\varphi_1-\varphi_2) \\ &\quad - a_1^3\rho r + a_1^3\rho r\cos(4t+4\varphi_1)\Big), \end{aligned} \tag{A.1}$$

$$\begin{aligned} &f_2(a_1,\varphi_1,a_2,\varphi_2,t) = \\ &\frac{1}{2a_1}\Big(-a_1 + 4a_1\rho\sin(2t+2\varphi_1) - a_1\cos(2t+2\varphi_1) \\ &\quad + a_2\cos(2t+\varphi_1+\varphi_2) + a_2\cos(\varphi_1-\varphi_2) \\ &\quad - 2a_1^3\rho r\sin(2t+2\varphi_1) + a_1^3\rho r\sin(4t+4\varphi_1)\Big), \end{aligned} \tag{A.2}$$

$$\begin{aligned} &f_3(a_1,\varphi_1,a_2,\varphi_2,t,\epsilon) = \\ &\frac{1}{8}\Big(-4a_2\mu + 4a_1\sin(2t+\varphi_1+\varphi_2) - 4a_1\sin(\varphi_1-\varphi_2) \\ &\quad + 4a_2\mu\cos(2t+2\varphi_2) - 4a_2\sin(2t+2\varphi_2) \\ &\quad + 2\alpha a_2^3\sin(2t+2\varphi_2) + \alpha a_2^3\sin(4t+4\varphi_2)\Big) \\ &+ \frac{\epsilon}{8}\Big[4a_1\rho\cos(\varphi_1-\varphi_2) - 4a_1\rho\cos(2t+\varphi_1+\varphi_2) \\ &\quad + 4a_1\sin(\varphi_1-\varphi_2) - 4a_1\sin(2t+\varphi_1+\varphi_2) \\ &\quad - 4a_2\mu + 4a_2\mu\cos(2t+2\varphi_2) + 4a_2\sin(2t+2\varphi_2) \\ &\quad + 2\alpha a_2^3\sin(2t+2\varphi_2) + \alpha a_2^3\sin(4t+4\varphi_2) \\ &\quad - a_1^3\rho r\cos(\varphi_1-\varphi_2) - a_1^3\rho r\cos(2t+3\phi_1-\phi_2) \\ &\quad + a_1^3\rho r\cos(2t+\phi_1+\phi_2) + a_1^3\rho r\cos(4t+3\phi_1+\phi_2)\Big] \end{aligned} \tag{A.3}$$

and

$$\begin{aligned} &f_4(a_1,\varphi_1,a_2,\varphi_2,t,\epsilon) = \\ &\frac{1}{8a_2}\Big(-4a_2 + 3\alpha a_2^3 \\ &\quad + 4\alpha a_2^3\cos(2t+2\varphi_2) + \alpha a_2^3\cos(4t+4\varphi_2) \\ &\quad + 4a_1\cos(2t+\varphi_1+\varphi_2) + 4a_1\cos(\varphi_1-\varphi_2) \\ &\quad - 4a_2\mu\sin(2t+2\varphi_2) - 4a_2\cos(2t+2\varphi_2)\Big) \\ &+ \frac{\epsilon}{8a_2}\Big[4a_2 + 3\alpha a_2^3 \\ &\quad - 4a_1\cos(2t+\varphi_1+\varphi_2) - 4a_1\cos(\varphi_1-\varphi_2) \\ &\quad + 4a_1\rho\sin(\varphi_1-\varphi_2) + 4a_1\rho\sin(2t+\varphi_1+\varphi_2) \\ &\quad + 4a_2\cos(2t+2\varphi_2) - 4a_2\mu\sin(2t+2\varphi_2) \\ &\quad + 4\alpha a_2^3\cos(2t+2\varphi_2) + \alpha a_2^3\cos(4t+4\varphi_2) \\ &\quad - a_1^3\rho r\sin(\varphi_1-\varphi_2) - a_1^3\rho r\sin(2t+3\phi_1-\phi_2) \\ &\quad a_1^3\rho r\sin(2t+\phi_1+\phi_2)\, a_1^3\rho r\sin(4t+3\phi_1+\phi_2)\Big]. \end{aligned} \tag{A.4}$$

Appendix B. General formulation of the standard stochastic averaging method

In this appendix the stochastic averaging method [31, 32] is briefly described. For that we consider the following system of differential equations in standard form

$$\dot{\mathbf{x}} = \mathbf{f}(\mathbf{x},t) + \mathbf{g}(\mathbf{x},t)\boldsymbol{\eta} \tag{B.1}$$

where $\mathbf{x} \in \mathbb{R}^n$. If the deterministic vector function $\mathbf{f}(\mathbf{x},t) \in \mathbb{R}^n$ and matrix function $\mathbf{g}(\mathbf{x},t) \in \mathbb{R}^n \times \mathbb{R}^n$ satisfy certain

requirements [32] and if the elements of the vector $\boldsymbol{\eta}$ are broadband processes, with zero means, then the slow (or averaged) dynamics of Eq. (B.1) may be approximated by the following stochastic differential equations

$$\dot{\mathbf{x}} = \mathbf{m}(\mathbf{x}, t) + \boldsymbol{\sigma}(\mathbf{x}, t)\boldsymbol{\xi}, \tag{B.2}$$

where $\boldsymbol{\xi} \in \mathbb{R}^n$ is a vector of n white noise processes with zero means. The vector $\mathbf{m}$ and the matrix $\boldsymbol{\sigma}$ are called *drift vector* and *diffusion matrix* respectively and are defined by

$$\mathbf{m} = M^{\text{av}} \left\{ \mathbf{f} + \int_{-\infty}^{0} \mathbb{E}\left[\left(\frac{\partial(\mathbf{g}\boldsymbol{\eta})}{\partial \mathbf{x}} \right)_t (\mathbf{g}\boldsymbol{\eta})_{t+s} \right] ds \right\}, \tag{B.3}$$

where $\frac{\partial(\mathbf{g}\boldsymbol{\eta})}{\partial \mathbf{x}}$ is the Jacobian matrix of $\mathbf{g}\boldsymbol{\eta}$, and

$$\boldsymbol{\sigma}\boldsymbol{\sigma}^T = M^{\text{av}} \left\{ \int_{-\infty}^{+\infty} \mathbb{E}\left[(\mathbf{g}\boldsymbol{\eta})_t (\mathbf{g}\boldsymbol{\eta})_{t+s}^T \right] ds \right\}, \tag{B.4}$$

where $\{.\}^T$ and $\mathbb{E}[\{.\}]$ denote respectively the transpose and the expected value of $\{.\}$. M^{av} is an averaging operator defined as follows

$$M^{\text{av}}\{.\} = \lim_{T \to +\infty} \frac{1}{T} \int_{t_0}^{t_0+T} \{.\}\, dt. \tag{B.5}$$

It should be noted that in the case of periodic variables with period T_0 (which is the case in this paper), the operator M^{av} becomes a classical Krylov–Bogolyubov time averaging over one period T_0, i.e.

$$M^{\text{av}}\{.\} = \frac{1}{T_0} \int_{t_0}^{t_0+T_0} \{.\}\, dt \tag{B.6}$$

and the result is independent of t_0.

Appendix C. Elements of the classical deterministic analysis of the slow flow dynamics

Combining Eqs. (30b) and (30c) leads to the following amplitude and angle equations

$$a_1 = a_2 \sqrt{\mu^2 + \left(1 - \frac{3\alpha a_2^2}{4}\right)^2} = H(a_2) \tag{C.1a}$$

$$\tan\varphi = \frac{4\mu}{4 - 3\alpha a_2^2}. \tag{C.1b}$$

As usual, the stability of the critical manifold is carried out studying the fast subsystem (31). A fixed point of Eq. (31) is shown to be stable if $d_{a_2}H(a_2) > 0$ and unstable if $d_{a_2}H(a_2) < 0$. Exploiting the polynomial properties of H, it can be shown that the local extrema of H (i.e $d_{a_2}H(a_2) = 0$) occur at

$$\begin{aligned} a_2^{\text{LF}} &= \frac{2}{3\sqrt{\alpha}} \sqrt{2 - \sqrt{1 - 3\mu^2}} \\ a_2^{\text{RF}} &= \frac{2}{3\sqrt{\alpha}} \sqrt{2 + \sqrt{1 - 3\mu^2}} \end{aligned} \tag{C.2}$$

if the following relation holds

$$\mu < \frac{1}{\sqrt{3}}. \tag{C.3}$$

If the condition (C.3) is not satisfied, the H function no longer has local extrema. In the rest of the paper, one considers that (C.3) always holds.

In Eq. (C.2), a_2^{LF} and a_2^{RF} are the abscissa values in the (a_2, a_1)-plane of the maximum and the minimum of the H function respectively. The superscripts $()^{\text{LF}}$ and $()^{\text{RF}}$ refer to *left fold point* and *right fold point* respectively. Indeed, in the (a_2, a_1, φ)-space, the two points $(a_2^{\text{RF}}, a_1^{\text{RF}}, \varphi^{\text{RF}})$ and $(a_2^{\text{LF}}, a_1^{\text{LF}}, \varphi^{\text{LF}})$ (where a_1^{LF}, a_1^{RF}, φ^{LF} and φ^{RF} are obtained from a_2^{LF} and a_2^{RF} using Eq. (C.1)) are generally called *fold points*.

Each point of the critical manifold is a fixed point of the fast subsystem (31). It can be shown that the stability of these fixed points changes at the fold points: they are stable (resp. unstable) for $a_2 < a_2^{\text{LF}}$ and $a_2 > a_2^{\text{RF}}$ (resp. $a_2^{\text{LF}} < a_2 < a_2^{\text{RF}}$).

Given the previous results, the critical manifold $\mathcal{M}_0$ is hyperbolic[3] except at the fold points and it consists of an attracting branch

$$\mathcal{M}_{0,\text{a}} = \left\{ (a_1, a_2, \varphi) \in \mathbb{R}^{+^2} \times [-\pi, \pi] \;\middle|\; a_2 < a_2^{\text{LF}} \text{ and } a_2 > a_2^{\text{RF}} \right\} \tag{C.4}$$

and a repelling branch

$$\mathcal{M}_{0,\text{r}} = \left\{ (a_1, a_2, \varphi) \in \mathbb{R}^{+^2} \times [-\pi, \pi] \;\middle|\; a_2^{\text{LF}} < a_2 < a_2^{\text{RF}} \right\}. \tag{C.5}$$

A typical amplitude part of the critical manifold (see Eq. (C.1a)) is shown in Fig. C.9. One can see that the fold points connect attracting parts to the repelling part of the critical manifold $\mathcal{M}_0$.

Solving $H\left(a_2^{\text{RF}}\right) = H\left(a_2^{\text{D}}\right)$ and $H\left(a_2^{\text{LF}}\right) = H\left(a_2^{\text{U}}\right)$ the two following scalars a_2^{D} and a_2^{U} are obtained

$$\begin{aligned} a_2^{\text{D}} &= \frac{2\sqrt{2}}{3\sqrt{\alpha}} \sqrt{1 - \sqrt{1 - 3\mu^2}} \\ a_2^{\text{U}} &= \frac{2\sqrt{2}}{3\sqrt{\alpha}} \sqrt{1 + \sqrt{1 - 3\mu^2}} \end{aligned} \tag{C.6}$$

which are the horizontal projection of the fold points on the critical manifold.

References

[1] O. V. Gendelman, L. I. Manevitch, A. F. Vakakis, R. M'Closkey, Energy Pumping in Nonlinear Mechanical Oscillators: Part I - Dynamics of the Underlying Hamiltonian Systems, Journal of Applied Mechanics 68 (1) (2001) 34. doi:10.1115/1.1345524.

[3] $\mathcal{M}_0$ is hyperbolic when all eigenvalues of the Jacobian of the fast susbsystem on $\mathcal{M}_0$ have nonzero real parts, here that means $d_{a_2}H(a_2) \neq 0$.

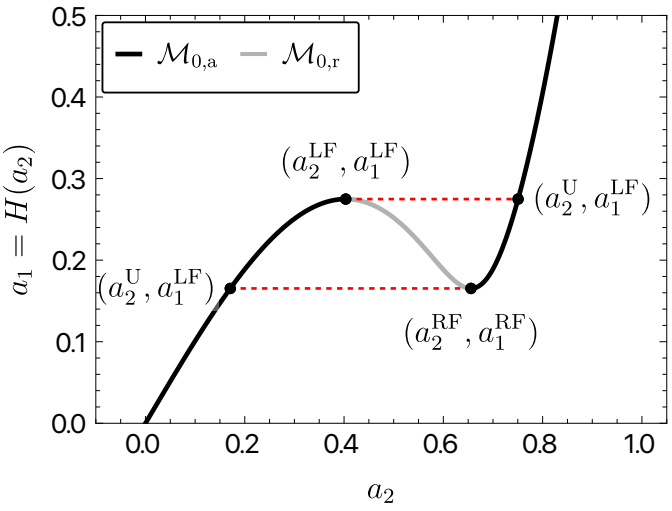

Figure C.9: Typical example of the critical manifold in the (a_2, a_1)-plane given by Eq. (C.1a) for $\mu = 0.25$ and $\alpha = 3$.

[2] A. F. Vakakis, O. V. Gendelman, Energy pumping in nonlinear mechanical oscillators: Part II - Resonance capture, Journal of Applied Mechanics 68 (2001) 42–48.

[3] A. F. Vakakis, O. V. Gendelman, L. A. Bergman, D. M. McFarland, G. Kerschen, Y. S. Lee, Nonlinear Targeted Energy Transfer in Mechanical and Structural Systems, 1st Edition, no. 156 in Solid Mechanics and Its Applications, Springer, 2009.

[4] Z. Lu, Z. Wang, Y. Zhou, X. Lu, Nonlinear dissipative devices in structural vibration control: A review, Journal of Sound and Vibration 423 (2018) 18–49.

[5] Y. S. Lee, A. F. Vakakis, L. A. Bergman, D. M. McFarland, Suppression of limit cycle oscillations in the van der Pol oscillator by means of passive non-linear energy sinks, Structural Control and Health Monitoring 13 (1) (2006) 41–75. doi:10.1002/stc.143.

[6] O. V. Gendelman, T. Bar, Bifurcations of self-excitation regimes in a Van der Pol oscillator with a nonlinear energy sink, Physica D 239 (3-4) (2010) 220–229. doi:10.1016/j.physd.2009.10.020.

[7] E. Domany, O. V. Gendelman, Dynamic responses and mitigation of limit cycle oscillations in van der pol-duffing oscillator with nonlinear energy sink, Journal of Sound and Vibration 332 (2013) 5489–5507.

[8] Y. S. Lee, A. F. Vakakis, L. A. Bergman, D. M. McFarland, G. Kerschen, Suppression aeroelastic instability using broadband passive targeted energy transfers, part 1: Theory, AIAA Journal 45 (3) (2007) 693–711. doi:10.2514/1.24062.

[9] Y. S. Lee, A. F. Vakakis, L. A. Bergman, D. M. McFarland, G. Kerschen, Suppression aeroelastic instability using broadband passive targeted energy transfers, part 2: Experiments, AIAA Journal 45 (3) (2007) 2391–2400. doi:10.2514/1.24062.

[10] Y. S. Lee, A. F. Vakakis, D. M. Bergman, L. A. McFarland, G. Kerschen, Enhancing the robustness of aeroelastic instability suppression using multi-degree-of-freedom nonlinear energy sinks, AIAA Journal 46 (6) (2008) 1371–1394.

[11] O. V. Gendelman, A. F. Vakakis, L. A. Bergman, D. M. McFarland, Asymptotic analysis of passive nonlinear suppression of aeroelastic instabilities of a rigid wing in subsonic flow, SIAM Journal on Applied Mathematics 70 (5) (2010) 1655–1677. doi:10.1137/090754819.

[12] A. Luongo, D. Zulli, Aeroelastic instability analysis of nes-controlled systems via a mixed multiple scale/harmonic balance method, Journal of Vibration and Control 20 (13) (2014) 1985–1998. doi:10.1177/1077546313480542.

[13] B. Bergeot, Scaling law for the slow flow of an unstable mechanical system coupled to a nonlinear energy sink, Journal of Sound and Vibration 503 (2021) 116109. doi:10.1016/j.jsv.2021.116109.

[14] R. K. R. Tumkur, E. Domany, O. V. Gendelman, A. Masud, L. A. Bergman, A. F. Vakakis, Reduced-order model for laminar vortex-induced vibration of a rigid circular cylinder with an internal nonlinear absorber, Communications in Nonlinear Science and Numerical Simulation 18 (7) (2013) 1916–1930. doi:10.1016/j.cnsns.2012.11.028.
URL http://dx.doi.org/10.1016/j.cnsns.2012.11.028

[15] H. L. Dai, A. Abdelkefi, L. Wang, Vortex-induced vibrations mitigation through a nonlinear energy sink, Communications in Nonlinear Science and Numerical Simulation 42 (2017) 22–36. doi:10.1016/j.cnsns.2016.05.014.

[16] A. T. Chirathalattu, B. Santhosh, C. Bose, R. Philip, B. Balaram, Passive suppression of vortex-induced vibrations using a nonlinear energy sink—numerical and analytical perspective, Mechanical Systems and Signal Processing 182 (1 2023). doi:10.1016/j.ymssp.2022.109556.

[17] B. Bergeot, S. Bellizzi, B. Cochelin, Analysis of steady-state response regimes of a helicopter ground resonance model including a non-linear energy sink attachment, International Journal of Non-Linear Mechanics 78 (2016) 72 – 89. doi:http://dx.doi.org/10.1016/j.ijnonlinmec.2015.10.006.

[18] B. Bergeot, S. Bellizzi, B. Cochelin, Passive suppression of helicopter ground resonance using nonlinear energy sinks attached on the helicopter blades, Journal of Sound and Vibration 392 (2017) 41–55. doi:10.1016/j.jsv.2016.12.039.

[19] B. Bergeot, S. Bellizzi, Asymptotic analysis of passive mitigation of dynamic instability using a nonlinear energy sink network, Nonlinear Dynamics 94 (2) (2018) 1501–1522. doi:10.1007/s11071-018-4438-0.

[20] B. Bergeot, S. Bellizzi, Steady-state regimes prediction of a multi-degree-of-freedom unstable dynamical system coupled to a set of nonlinear energy sinks, Mechanical Systems and Signal Processing 131 (2019) 728–750.

[21] B. Bergeot, S. Bellizzi, S. Berger, Dynamic behavior analysis of a mechanical system with two unstable modes coupled to a single nonlinear energy sink, Communications in Nonlinear Science and Numerical Simulation 95 (2021) 105623. doi:10.1016/j.cnsns.2020.105623.

[22] E. Gourdon, C.-H. Lamarque, Nonlinear energy sink with uncertain parameters, Journal of computational and nonlinear dynamics 1 (3) (2006) 187–195.

[23] E. Cataldo, S. Bellizzi, R. Sampaio, Free vibrations of an uncertain energy pumping system, Journal of Sound and Vibration 332 (25) (2013) 6815–6828. doi:10.1016/j.jsv.2013.08.022.

[24] E. Boroson, S. Missoum, P.-O. Mattei, C. Vergez, Optimization under uncertainty of parallel nonlinear energy sinks, Journal of Sound and Vibration 394 (2017) 451–464. doi:10.1016/j.jsv.2016.12.043.
URL http://linkinghub.elsevier.com/retrieve/pii/S0022460X16308045

[25] B. Pidaparthi, S. Missoum, Stochastic optimization of nonlinear energy sinks for the mitigation of limit cycle oscillations, AIAA Journal (2019) 1–11doi:10.2514/1.j057897.

[26] C. Snoun, B. Bergeot, S. Berger, Prediction of the dynamic behavior of an uncertain friction system coupled to nonlinear energy sinks using a multi-element generalized polynomial chaos approach, European Journal of Mechanics - A/Solids 80 (2020) 103917. doi:https://doi.org/10.1016/j.euromechsol.2019.103917.
URL http://www.sciencedirect.com/science/article/pii/S0997753819307132

[27] C. Snoun, B. Bergeot, S. Berger, Robust optimization of nonlinear energy sinks used for mitigation of friction-induced limit cycle oscillations, European Journal of Mechanics - A/Solids 93 (2022) 104529. doi:10.1016/j.euromechsol.2022.104529.
URL https://doi.org/10.1016/j.euromechsol.2022.104529

[28] F. Schmidt, C. H. Lamarque, Computation of the solutions of the fokker-planck equation for one and two dof systems, Communications in Nonlinear Science and Numerical Simulation 14 (2009) 529–542. doi:10.1016/j.cnsns.2007.09.004.

[29] Y. Starosvetsky, O. V. Gendelman, Response regimes in forced system with non-linear energy sink: Quasi-periodic and random forcing, Nonlinear Dynamics 64 (2011) 177–195. doi:10.1007/s11071-010-9856-6.

[30] T. P. Sapsis, A. F. Vakakis, L. A. Bergman, Effect of stochasticity on targeted energy transfer from a linear medium to a strongly nonlinear attachment, Probabilistic Engineering Mechanics 26 (2) (2011) 119 – 133. doi:https://doi.org/10.1016/j.probengmech.2010.11.006.
URL http://www.sciencedirect.com/science/article/pii/S0266892010000998

[31] R. L. Stratonovich, Topics In the Theory of Random Noise, Vol. 1, Taylor & Francis, 1963, Ch. 4.

[32] R. Z. Khas'minskii, A Limit Theorem for the Solutions of Differential Equations with Random Right-Hand Sides, Theory of Probability & Its Applications 11 (3) (1966) 390–406. doi:10.1137/1111038.

[33] J. B. Roberts, P. D. Spanos, Stochastic averaging: An approximate method of solving random vibration problems, International Journal of Non-Linear Mechanics 21 (2) (1986) 111–134. doi:10.1016/0020-7462(86)90025-9.

[34] G. S. Fishman, Monte carlo: concepts, algorithms, and applications, Springer Series in Operations Research, Springer, New York, 1996.
URL http://cds.cern.ch/record/1614885

[35] B. Øksendal, Stochastic Differential Equations: An Introduction with Applications, Springer, 2003.

[36] A. H. Nayfeh, D. T. Mook, Nonlinear Oscillations, John Wiley & Sons, Ltd, 1995.

[37] L. Manevitch, Complex representation of dynamics of coupled nonlinear oscillators, in: L. Uvarova, A. Arinstein, A. Latyshev (Eds.), Mathematical Models of Non-Linear Excitations, Transfer, Dynamics, and Control in Condensed Systems and Other Media, Springer US, 1999, pp. 269–300. doi:10.1007/978-1-4615-4799-0_24.

[38] Wolfram Research, Inc., Mathematica, Version 13.1, champaign, IL, 2022.
URL https://www.wolfram.com/mathematica

[39] M. Desroches, J. Guckenheimer, B. Krauskopf, C. Kuehn, H. Osinga, M. Wechselberger, Mixed-mode oscillations with multiple time scales, SIAM Review 52 (2) (2012) 211–288. doi:10.1137/100791233.

[40] B. Bergeot, S. Berger, Solution analytique d'une bifurcation col-noeud dynamique : application à la prédiction de la limite de fonctionnement d'un absorbeur non linéaire de type nes pour l'atténuation de cycles limites, in: 15e Colloque National de Calcul des Structures, CSMA, 2022.

[41] N. Berglund, B. Gentz, Berglund, Gentz - 2006 - Noise-induced phenomena in slow-fast dynamical systems a sample-paths approach, Springer London, 2006. doi:https://doi.org/10.1007/1-84628-186-5.

[42] N. Berglund, B. Gentz, Stochastic Dynamic Bifurcations and Excitability, in: Stochastic Methods in Neuroscience, Oxford Scholarship Online, 2010. doi:10.1093/acprof:oso/9780199235070.003.0003.